Int. J. Radiation Oncology Biol. Phys., Vol. 76, No. 2, pp. 583–596, 2010

0360-3016/10/$–see front matter

ELSEVIER

doi:10.1016/j.ijrobp.2009.06.031

PHYSICS CONTRIBUTION

RESULTS OF A MULTI-INSTITUTION DEFORMABLE REGISTRATION ACCURACY STUDY (MIDRAS)

KRISTY K. BROCK, PH.D., ON BEHALF OF THE DEFORMABLE REGISTRATION ACCURACY CONSORTIUM

Princess Margaret Hospital, University Health Network, Departments of Radiation Oncology and Medical Biophysics, University of Toronto, Toronto, Ontario, Canada

Purpose: To assess the accuracy, reproducibility, and computational performance of deformable image registration algorithms under development at multiple institutions on common datasets.

Methods and Materials: Datasets from a lung patient (four-dimensional computed tomography [4D-CT]), a liver patient (4D-CT and magnetic resonance imaging [MRI] at exhale), and a prostate patient (repeat MRI) were obtained. Radiation oncologists localized anatomic structures for accuracy assessment. Algorithm accuracy was determined by comparing the computer-predicted displacement at each bifurcation point with the displacement computed from the oncologists' annotations. Thirty-seven academic institutions and medical device manufacturers with published evidence of active deformable image registration capabilities were invited to participate.

Results: Twenty-seven groups agreed to participate; 6 did not return results. Sixteen completed the liver 4D-CT, 12 the lung 4D-CT, 3 the prostate MRI, and 3 the liver MRI-CT. The range of average absolute error for the lung 4D-CT was 0.6–1.2 mm (left–right [LR]), 0.5–1.8 mm (anterior–posterior [AP]), and 0.7–2.0 mm (superior–inferior [SI]); the liver 4D-CT was 0.8–1.5 mm (LR), 1.0–5.2 mm (AP), and 1.0–5.9 mm (SI); the liver MRI-CT was 1.1–2.6 mm (LR), 2.0–5.0 mm (AP), and 2.2–2.6 mm (SI); and the repeat prostate MRI prostate datasets was 0.5–6.2 mm (LR), 3.1–3.7 mm (AP), and 0.4–2.0 mm (SI).

Conclusions: An infrastructure was developed to assess multi-institution deformable registration accuracy. The results indicate large discrepancies in reported shifts, although the majority of deformable registration algorithms performed at an accuracy equivalent to the voxel size, promising to improve treatment planning, delivery, and assessment.

Deformable registration, Multi-institution study, Lung, Liver, Prostate.

Reprint requests to: Kristy K. Brock, PhD., 610 University Ave, Room 7-502A, Toronto, Ontario, Canada, M5G 2M9. Tel: (416) 946-4501 x6565; Fax: (416) 946-6566; E-mail: kristy.brock@rmp.uhn.on.ca

Supported in part by the Connaught New Staff Grant through the University of Toronto.

Conflict of interest: none.

Acknowledgment—The principal investigator thanks Joanne Moseley, who performed the data analysis; Laura Dawson, Cynthia Menard, Andrea Bezjak, Charles Catton, and Kevin Franks, who provided clinical data and identified anatomic points; and Michael Sharpe, Douglas Moseley, and Gavin Disney, who assisted with data exporting. The principal investigator especially thanks the participants who made this multi-institution study possible, the Deformable Registration Accuracy Consortium, consisting of the following: Karsten Noe and Kari Tanderup, Department of Radiation Oncology, Aarhus University Hospital, Aarhus, Denmark; Xiao Han, CMS Software, Elekta Inc., St. Louis, MO, USA; Issam El Naqa and Deshan Yang, Department of Radiation Oncology, Washington University, St. Louis, MO, USA; Mark Foskey and Ed Chaney, Department of Radiation Oncology, University of North Carolina, Chapel Hill, NC, USA; David Hawkes and William Crum (now at Centre for NeuroImaging Sciences, Kings College London), Centre for Medical Image Computing, University College London, London, UK; David Sarrut and Vlad Boldea, Centre de Lutte Contre le Cancer Léon Bérard and CREATIS-LRMN laboratory, Lyon University, France; Emily Heath, Medical Physics Unit, McGill University, Montreal, Quebec, Canada; Lei Dong and Lifei Zhang, The University of Texas M. D. Anderson Cancer Center, Houston, TX, USA; Gig Mageras and Yu-Chi Hu, Medical Physics Department, Memorial Sloan-Kettering Cancer Center, New York, NY, USA, Michael Kaus and Torbjoern Vik, Philips Medical Systems, Madison, WI, USA; Thao-Nguyen Nguyen, Radiation Medicine Program, Princess Margaret Hospital, Toronto, Ontario, Canada; Gregory Sharp, Department of Radiation Oncology, Massachusetts General Hospital, Boston, MA, USA; Frank Van den Heuvel and Pieter Slagmolen, Oncology and Experimental Radiotherapy, University Hospitals K.U. Leuven, Leuven, Belgium; Anne Nord, Varian Medical Systems, Palo Alto, CA, USA; John Lee, Pierre Castadot, and Adriane Parraga, Université Catholique de Louvain, St-Luc University Hospital, Louvain-la-Neuve, Belgium; Raj Shekhar and Jianzhou Wu, Department of Diagnostic Radiology, University of Maryland, Baltimore, MD, USA; David Hawkes and Jamie McClelland, Centre for Medical Image Computing, University College London, London, UK; Jan-Jakob Sonke and Jochem Wolthaus, Department of Radiation Oncology, The Netherlands Cancer Institute-Antoni van Leeuwenhoek Hospital, Amsterdam, The Netherlands; Tiezhi Zhang and Yuwei Chi, Department of Radiation Oncology, William Beaumont Hospital, Royal Oak, MI, USA; Paul Dufort and Audrius Stundzia, Tomographix IP Ltd, Toronto, Ontario, Canada; and Junyi Xia and Sanjiv Samant, Department of Radiation Oncology, University of Florida, Gainesville, FL, USA.

Received Jan 5, 2009, and in revised form June 1, 2009. Accepted for publication June 3, 2009.

INTRODUCTION

In recent years, the incorporation of multimodality, multi-instance imaging in treatment planning for external beam radiotherapy and three-dimensional soft tissue imaging for daily image guidance has significantly increased. These advances have indicated the potential to reduce treatment margins accommodating uncertainties in tumor extent, motion, and position at time of treatment relative to planning position by increasing the geometric consistency and understanding of the patient throughout the treatment process. Reduced treatment margins lead to less volume of normal tissues irradiated, resulting in a reduced risk of normal tissue toxicity after radiation and the potential to deliver higher doses safely to the tumor, potentially leading to increased tumor control probability. Sequential three-dimensional and four-dimensional (4D) imaging highlights the obvious nonrigid nature of the motion of the human body. Short-term motion, characterized using dynamic or ciné imaging and long-term motion, identified using multi-instance imaging, both identify the need for deformable registration to accommodate the complex physiologic motion and changes in anatomy caused by treatment interventions.

Several methods of image registration are currently available, both commercially and in research environments. The majority of commercially available registration methods include only rigid body motion. Although sufficient for some anatomic sites, such as the brain, rigid body registration fails in the registration of temporal imaging of physiologic motion and tumor and normal tissue response (1–7). Several deformable image registration algorithms are currently under investigation and have been developed and reported on in the literature However, algorithmic accuracy has been tested inconsistently, test cases are usually limited to a narrow range of clinical situations (*e.g.,* imaging modality, disease site), and reported errors vary widely for similar methods. This confounds the ability to objectively benchmark algorithms and will hinder the widespread adoption of such algorithms into clinical practice (1, 5, 6, 8–20). Each algorithm has its benefits and limitations, and it is likely that the variations in clinical scenarios will benefit from the differences in algorithms. Recently, a multi-institution study was conducted on a 4D phantom, showing acceptable overall results but the potential for large errors in regions with large deformations (21). In addition, a 4D computed tomography (CT) image

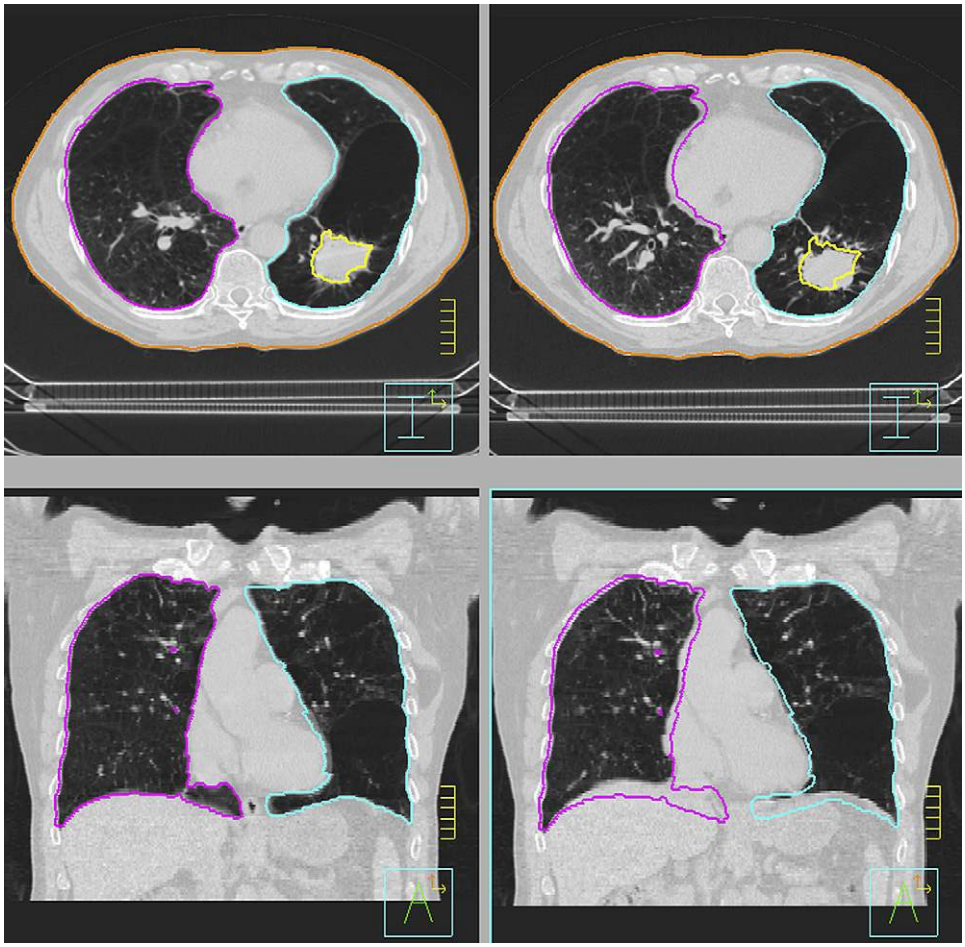

Fig. 1. Inhale, 0% phase (left) and exhale, 50% phase (right) reconstructions from the four-dimensional computed tomography images obtained for the example lung patient. The lungs (purple and aqua) and tumor (yellow) are contoured on the inhale image and overlaid onto the exhale image for reference.

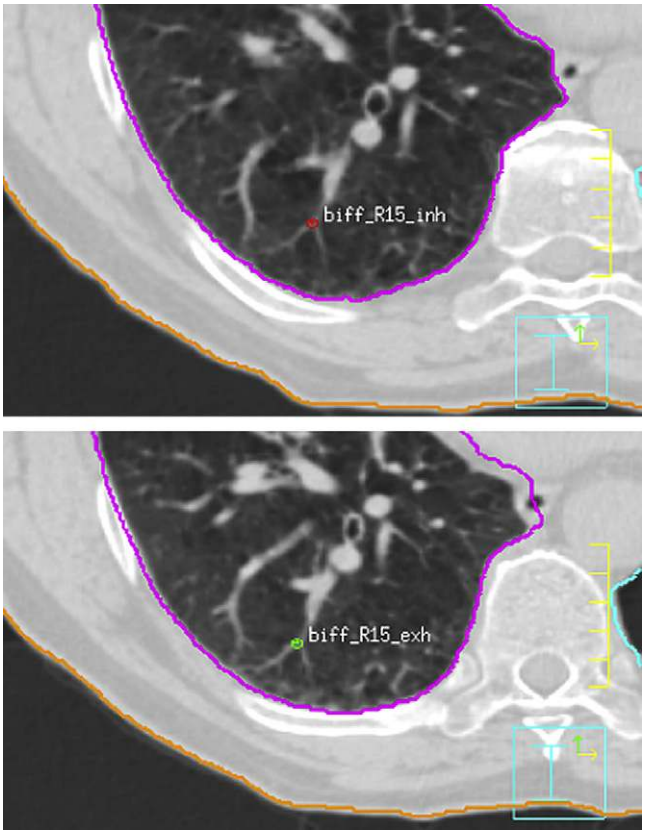

Fig. 2. Example of the corresponding bronchial bifurcations identified in the inhale (top) and exhale (bottom) images.

set with point-validated motion models and also expert-based validation data has been made available by Vandemeulebroucke *et al*. (22).

The objective of this research is to provide a consistent quantitative metric of accuracy, allowing direct comparison of the various algorithms, and to provide an indication of performance by applying and analyzing algorithms for a selected number of test cases. Once these objectives are reached, the limitations of the currently developed algorithms can be assessed and baseline accuracy can be established to aid in the integration of deformable registration algorithms when they become available clinically, either commercially or through research collaborations.

METHODS AND MATERIALS

Data

Patient images were retrospectively obtained under a research ethics board—approved study. Three anatomic sites were studied: lung, liver, and prostate. The data are described below.

Lung. Respiration-correlated 4D-CT, data were obtained for 1 lung patient using a Varian RPM system on a GE Medical Systems CT scanner. A coronal and axial reconstruction is shown in Fig. 1. The image set was 512 x 512 x 152 with an in-plane pixel size of 0.98 x 0.98 mm and a slice thickness of 2.5 mm. The datasets at 0% and 50% breathing phases were imported into a treatment planning system (Pinnacle v 7.6c, Philips Healthcare) for contouring. The external of the patient, right and left lungs and tumor were delineated on the inhale, 0%, dataset. The external and right and left lungs were delineated on the exhale, 50%, dataset. The contours were exported from the planning system as a DICOM-RT structure. The DICOM images and the DICOM RT structure set were sent to each participant.

To perform quantitative analysis of the deformable registration accuracy, a radiation oncologist experienced in treating lung cancer identified corresponding naturally occurring fiducial markers in each image. Seventeen bronchial bifurcations were identified in the right lung, 17 bronchial bifurcations in the left lung, 2 calcifications in the heart, and 2 calcifications in the aorta. An example of the bronchial bifurcations identified is shown in Fig. 2. The motion of the bifurcations in the thorax are shown in Table 1.

Liver. Respiration correlated, 4D-CT, data were obtained for 1 liver patient using a Varian RPM system (Varian Medical Systems, Palo Alto, CA) on a GE LightSpeed plus 16-slice scanner (General Electric, Milwaukee, WI). A coronal and axial reconstruction is shown in Fig. 3. Intravenous contrast medium (Visipaque 270, Amershamhealth) was delivered before image acquisition. The image set was 512 × 512 × 120 with an in-plane pixel size of 0.98 × 0.98 mm and a slice thickness of 2.5 mm. The 0% and 50% datasets were imported into a treatment planning system (Pinnacle v7.6c, Philips Healthcare) for contouring. The external of the patient, liver, kidneys, bowel, duodenum, esophagus, and tumor were contoured on the exhale dataset per clinical practice. The external and liver were also contoured on the inhale data. The contours were exported from the planning system as DICOM-RT structures.

In addition, corresponding naturally occurring fiducial markers were identified on each image by a radiation oncologist experienced in treating liver cancer to perform quantitative analysis of the accuracy. Twenty-five vessel bifurcations were identified in the liver, five vessel bifurcations were identified in the left kidney, and six vessel bifurcations were identified in the right kidney. An example

Table 1. Motion of the bifurcations in the thorax, mean (SD), range (mm)

	LR	AP	SI
Right lung	−0.5 (1.0) −2.0 to 1.0	1.6 (1.2) 0 to 4.9	2.1 (4.0) 0 to 15.0
Left lung	−1.1 (1.6) −2.9 to 1.0	−1.0 (2.1) −2.9 to 4.9	4.1 (4.8) 0 to 15.0
Heart calcification 1	−3.9	2.9	5.0
Heart calcification 2	−3.9	0	5.0
Aorta calcification 1	−1.0	−1.0	0
Aorta calcification 2	−5.9	0	2.5

Abbreviations: LR = left–right; AP = anterior–posterior; SI = superior–inferior.

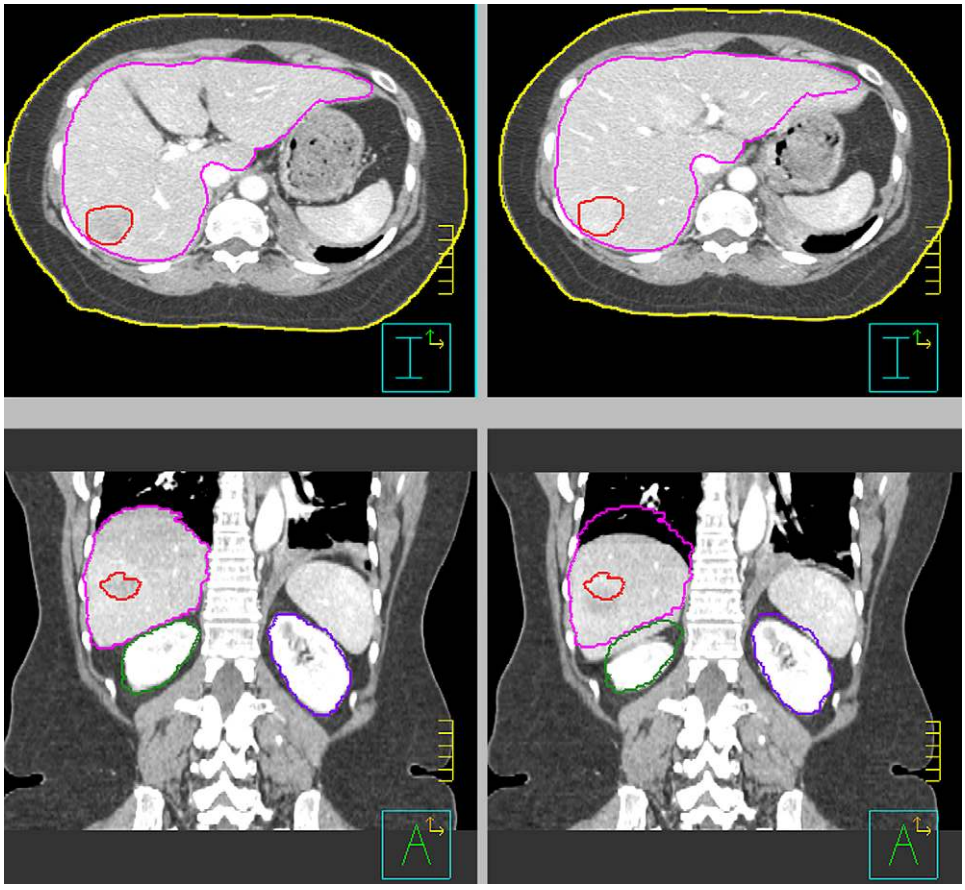

Fig. 3. Exhale, 50% phase (left) and inhale, 0% phase (right) reconstructions from the four-dimensional computed tomography images obtained for the example liver patient. The liver (pink), tumor (red), and kidneys (green and purple) contoured on the exhale images are overlaid onto the inhale images for reference.

of the vessel bifurcation in the liver is shown in Fig. 4. The motion of the bifurcations in the liver and kidneys is shown in Table 2.

Additionally, voluntary exhale breath-hold magnetic resonance imaging (MRI) was performed on the same patient on a GE 1.5 Tesla TwinSpeed MRI simulator platform (General Electric) using a spoiled gradient echo imaging sequence. A coronal and axial reconstruction is shown in Fig. 5. The image set was 256 × 256 × 24 with an in-plane pixel size of 1.7 × 1.7 mm and a slice thickness of 7.0 mm. The external of the patient and the liver was contoured, and the contours were exported from the planning system as DICOM RT structures.

Seven pairs of vessel bifurcations were identified in the liver between the exhale sorted 4D-CT and the exhale breath-hold MRI, and an example is shown in Fig. 6. The average motion of the bifurcations was 15.4 mm (SD, 2.5 mm; range, 12.7–19.6 mm) in the left–right (LR) direction, 10.9 mm (SD, 1.6 mm; range, 9.0–13.0 mm) in the anterior–posterior (AP) direction, and 71.3 mm (SD, 2.7; range, 68.8–76.3 mm) in the superior–inferior (SI) direction. These motions are larger because they include a large rigid translation component caused by patient positioning.

Prostate. Repeat prostate MRIs were obtained on a GE 1.5 Tesla TwinSpeed MRI simulator platform using a gradient recalled echo sequence. An axial reconstruction of both images is shown in Fig. 7. The image set was 256 × 256 × 29 with an in-plane resolution of 0.70 × .70 mm and a slice thickness of 2 mm. Before image acquisition, the patient had 3 gold seeds (1 × 5 mm) implanted in the prostate. Both images were imported into the treatment planning system. A radiation oncologist, experienced in treating prostate cancer, contoured the prostate, rectum, and bladder on each image and also the three gold seeds. A point was automatically placed at the center of mass of each contoured seed. The average motion of the seeds was 9.8 mm (SD, 0.7 mm; range, 9.0–10.3 mm) in the LR direction, 18.3 mm (SD 3.6; range, 14.4–21.5 mm) in the AP direction, and 48.3 mm (SD, 2.0 mm; range, 47.7–50.5 mm) in the SI direction. The large displacements represent the global rigid registration required between the two imaging sessions; however, note the substantial range in the AP direction, which indicates deformation between the two imaging sessions.

Deformable registration instructions

Each institution participating in the study was asked to perform deformable registration between primary and the secondary datasets for 4D-CT liver (exhale to inhale), 4D-CT lung (inhale to exhale), MR prostate (two repeat scans), and MR liver to CT liver. Participants were asked to summarize the method used to deform the images and to record their processing times.

To evaluate the success of the image registration, participants generated a set of deformation matrices in the same coordinate system as the primary dataset. The value in each voxel in the deformation matrix is the displacement required at the center of that voxel to deform the primary dataset to the secondary. Three deformation matrices were generated, one for each cardinal direction.

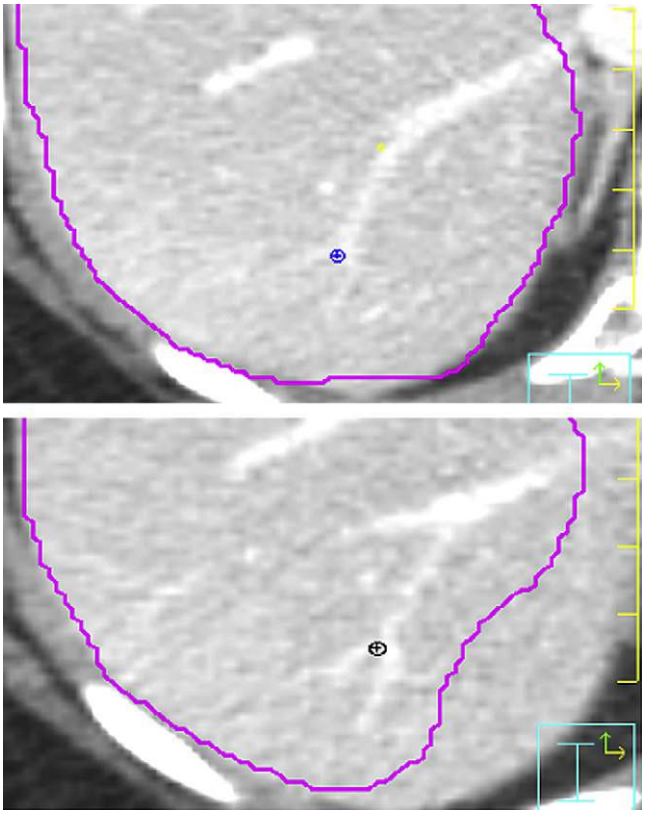

Fig. 4. Example of the corresponding vessel bifurcations identified in the exhale (top) and inhale (bottom) images. The liver (purple) contoured on the exhale image is overlaid onto the inhale image.

Registration validation

Validation was performed by identifying corresponding fiducials in the primary organ of interests on the primary and secondary datasets. These included bronchial bifurcations in the lung, vessel bifurcations in the liver, and implanted gold marks in the prostate. Fiducials were also identified in secondary organs of interest (*i.e.,* heart, aortas, and kidneys) as visible on the images. The displacement of these fiducials was taken to be the true displacement of the organs to which the participant's results were compared.

The location of the fiducial points was interpolated onto the deformation grid using bilinear interpolation. The value of the voxel in the deformation matrix at that location was compared with the actual displacement at that point as described by the fiducial points and the error calculated. Participants received a summary of their results, which included a list of the fiducial points, the actual displacement at each point, the displacement that their algorithm reported based on the returned deformation maps, the difference between their result at each point and the actual displacement (error), and the absolute value of the differences (absolute error). The mean and standard deviation of the errors over all points was calculated. Each institution also received a blind summary of the results showing the mean error and standard deviation for each institution so they could compare the results of their algorithm with others.

Registration algorithms

The participants were required to return their data by August 31, 2007, if they wanted to participate in the study. A summary of the primary investigators, institution or company, and key registration parameters is shown in Table 3, along with references.

Table 2. Motion of the bifurcations in the liver and kidneys, mean (SD), range (mm)

	LR	AP	SI
Liver	−0.7 (1.4) −3.9 to 2.0	−4.1 (2.2) −8.8 to 2.9	−11.9 (1.9) −7.5 to −15.0
Kidneys	−0.8 (1.4) −2.9 to 1.0	−3.2 (2.9) −6.8 to 1.0	−7.3 (3.8) −2.5 to −12.5

Abbreviations: LR = left–right; AP = anterior–posterior; SI = superior–inferior.

RESULTS

Data collection

Twenty-two participants returned data for the lung 4D-CT study, 17 participants returned data for the liver 4D-CT study, four participants returned data for the liver MR-CT study, and four participants returned data for the prostate study.

Lung 4D-CT

Lung. All algorithms had a mean absolute error of less than 2.5 mm, which is equal to the slice thickness of the image set. Twenty of the algorithms also had a standard deviation of less than 2.5 mm. The largest mean absolute error was 2.0 mm. Nine algorithms had a maximum error of less than 5.0 mm in each direction. Seventeen algorithms had maximum errors of less than 7.5 mm in each direction. The maximum error across all algorithms was 1.2 cm. Summaries of the results are shown in Table 4.

Heart and aorta. Seventeen algorithms had an absolute mean error of less than 2.5 mm in each direction; the remaining four had absolute errors of less than 5.0 mm. Thirteen algorithms had an absolute standard deviation of less than 2.5 mm in each direction; the remaining eight had a standard deviation of less than 5.0 mm. Eighteen algorithms had a maximum error in the heart and aorta of greater than 5.0 mm; the maximum error was 6.7 mm. Summaries of the results are shown in Table 4.

Liver 4D-CT

Liver. Seven algorithms had a mean absolute error in the liver of less than 2.5 mm in each direction (equal to the slice thickness). Twelve algorithms had an absolute standard deviation of less than 2.5 mm in each direction. Eight algorithms had a mean absolute error of less than 5.0 mm in each direction, and one algorithm had a mean absolute error of less than 7.5 mm in each direction. All algorithms had a maximum error of greater than 5.0 mm in at least 1 direction. Three algorithms had a maximum error of greater than 1 cm, occurring in the SI direction. Summaries of the results are shown in Table 5.

Left kidney. Sixteen algorithms had a mean absolute error and absolute standard deviation of less than 2.5 mm in each direction. All algorithms had a mean absolute error and absolute standard deviation of less than 3.0 mm in each direction. Fifteen algorithms had a maximum error of less than 2.5 mm,

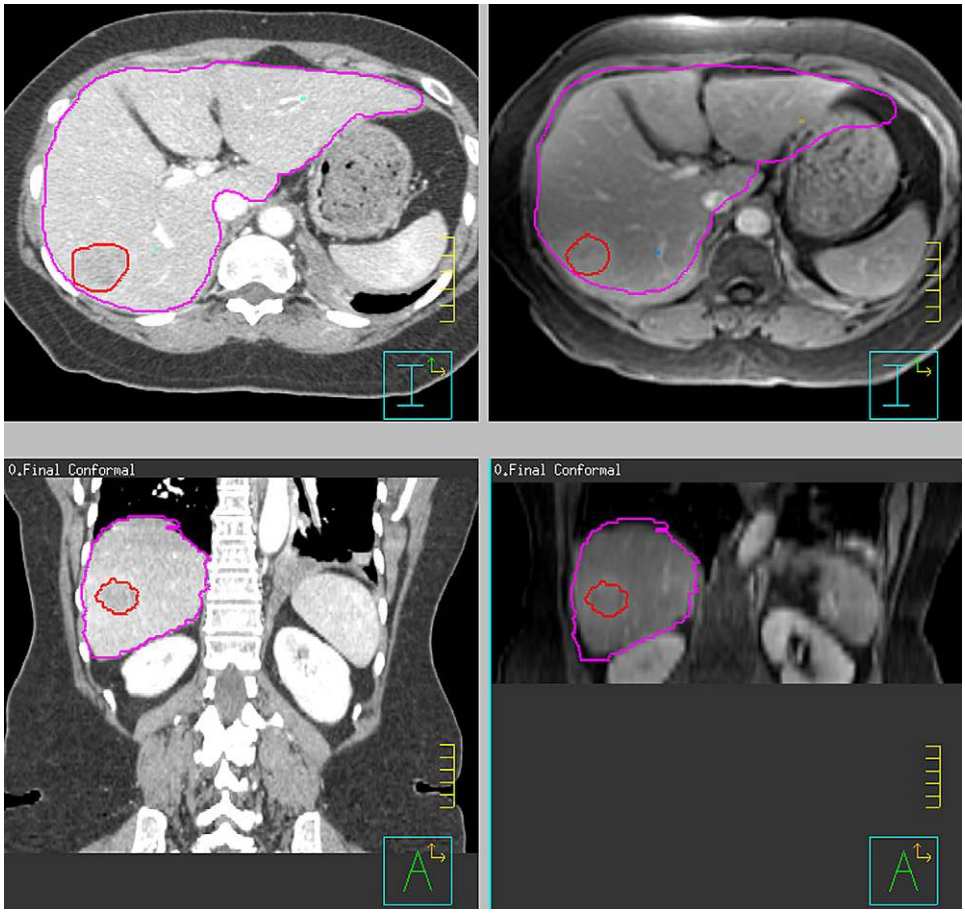

Fig. 5. Exhale, 50% phase reconstruction from the four-dimensional computed tomography (left) voluntary exhale breath hold magnetic resonance images (right) obtained for the example liver patient. The liver (pink) and tumor (red) contoured on the exhale images are overlaid onto the magnetic resonance images for reference.

and the maximum error for all algorithms was 3.3 mm. Summaries of the results are shown in Table 5.

Right kidney. Eleven algorithms had a mean absolute error of less than 2.5 mm in each direction. Four algorithms had a mean absolute error of less than 3.5 mm in each direction. All algorithms had an absolute standard deviation of less than 2.5 mm in each direction. Four algorithms had a maximum error of less than 2.5 mm in all directions. Ten algorithms had a maximum error of less than 5.0 mm in all directions. The maximum error in the right kidney was 5.6 mm. Summaries of the results are shown in Table 5.

Liver MRI-CT

Three investigators submitted results for the MR-CT liver registration. The mean absolute error for the liver ranged from 1.1 to 5.0 mm, with the SI direction having the worst error for one algorithm and the AP direction having the worst error for two algorithms. The absolute standard deviations were less than 2.5 mm for all three algorithms. The maximum error was less than 7.0 mm for all three algorithms. Summaries of the results are shown in Table 6.

Prostate

Three investigators submitted results for the repeat MRIs of the prostate. The mean absolute error for the prostate ranged from 0.4 to 6.2 mm, with the largest error in the LR (one algorithm) and AP (two algorithms) directions. The absolute standard deviations ranged from 0.3 to 3.4 mm. The maximum errors ranged from 5.0 to 8.7 mm. Summaries of the results are shown in Table 7.

Algorithm efficiency

The times required for the algorithms to complete ranged from 45 s to more than 10 hours. This large variation indicates the potential for near real-time deformable registration, which may be suitable for online image guidance, and also indicates the need for algorithm optimization. Efficiency varied across algorithm implementation (*i.e.*, different institutions using the same algorithm basis). For example, four implementations of B-spline ranged from 12 minutes to 10.3 hours. Implementation of the Demons algorithms tended to have the best efficiency, ranging from 45 s to 60 min.

Efficiency did not seem to come at the expense of accuracy. For the three algorithms that did not have a maximum error of greater than 5 mm, the algorithm efficiency ranged

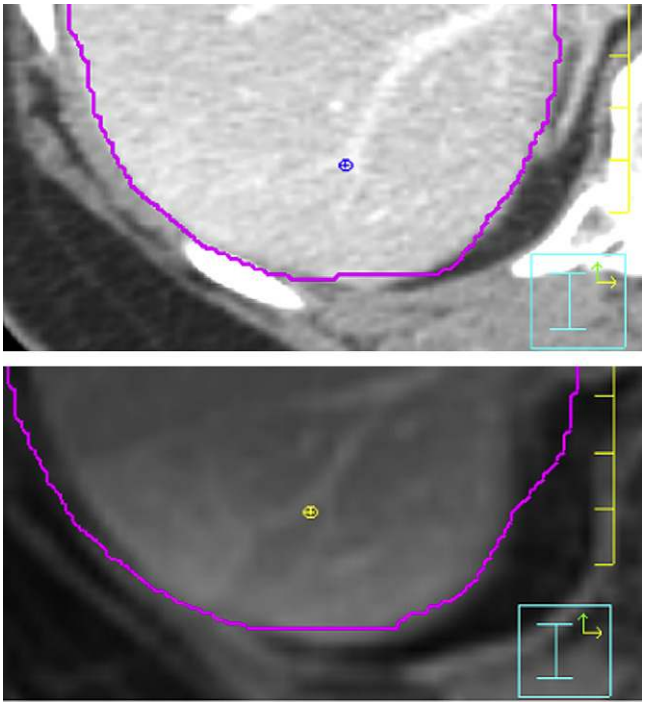

Fig. 6. Example of the corresponding vessel bifurcations identified in the exhale computed tomography (top) and magnetic resonance (bottom) images. The liver (purple) contoured on the exhale image is overlaid onto the magnetic resonance image.

from 2 min to 1 hour. For the seven algorithms that did not have a maximum error of greater than 7 mm, the algorithm efficiency ranged from 3 min to 5 hours.

DISCUSSION

A multi-institutional deformable registration study was successfully performed to evaluate the accuracy of several algorithms using a common set of clinical data from human patients. Naturally occurring landmarks were used for validation in the thorax and abdomen, with implanted markers serving as validation points in the prostate.

It should be noted that the data used in this study were clinical data obtained from patients who had previously been studied. Efforts were made to find 4D-CT data that exhibited ''typical'' motion caused by respiration with minimal artifacts. However, the data were not perfect, and some artifacts did exist. These errors were in the 4D reconstruction of the breathing data, where the correlation between the respiration surrogate and the internal anatomy was not consistent, manifesting itself, for example, as disconnected pieces of the liver. Although efforts should be made to reduce or eliminate these artifacts in clinical practice, in the clinical setting artifacts will exist. It was the goal of this study to examine the accuracy of deformable registration algorithms on data that are typically seen in the clinical setting.

Although the study was limited in the number of datasets, several observations can be made; however' complete conclusions on the robustness of the algorithms will require additional testing on multiple datasets.

All algorithms performed well for lung 4D-CT, with mean absolute errors of less than or equal to 2.5 mm in each direction. This is likely due to the consistent contrast between the two images. The large maximum errors, up to 12.0 mm, should be noted. The effect of these large errors may be more forgiving in dose accumulation applications if gradients are not sharp, but if these errors exist near the tumor, their effect on image-guidance applications may be clinically significant.

Most algorithms performed well for the liver 4D-CT, with most mean absolute errors less than 2.5 mm. The large maximum errors, up to 13.0 mm, should also be noted. These large errors may be especially concerning for the liver, where the tumor is typically not visible on volumetric imaging without the use of contrast medium. It should also be noted that not all algorithms that performed the deformable registration on the lung 4D-CT dataset returned results for the liver, highlighting the need to continue working on expanding the application of deformable registration in other anatomic sites.

Very few algorithms reported results for the multimodality liver images, primarily because of the algorithm's inability to

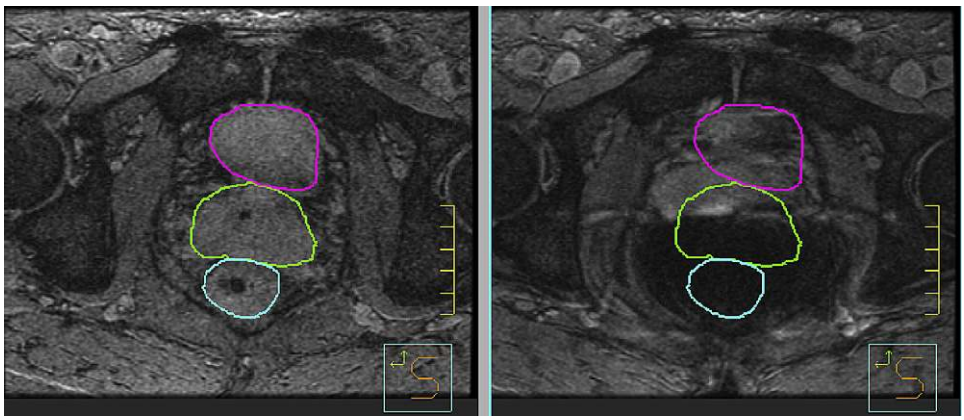

Fig. 7. Repeat magnetic resonance images obtained for the example prostate patient. The bladder (pink), prostate (green), and rectum (blue) contoured on the first image (left) are overlaid onto the second magnetic resonance image (right) for reference.

Table 3. List of participants: study number, institution, investigator, similarity metric used, interpolation method, optimization, and references

Study no.	Institution	Investigator	Similarity metric	Regularization method	Optimization	Time (m)	Computer	Reference
1	Aarhus	Noe, Tanderup	SSD	Viscous-fluid	GPU accelerated gradient descent	3.5–4.3	PD, 3.0 GHz, 2 GB RAM, GeForce 7900GTX 512 MB DDRIII video RAM	23
2	CMS	Han	SSD	Free-form with spatial smoothing	Multi-resolution gradient-decent	10–14	P4, 3.2 GHz, 3 GB RAM	24, 25
3	Washing University St. Louis	El Naqa, Yang	MSD	Horn-Schunck optical flow	Multiresolution with Gauss–Seidel iterations	10–16	Xeon, 3.0 GHz, 3 GB RAM	26
4	U of North Carolina	Foskey, Chaney	SSD	Viscous fluid flow	Multiscale, regularized gradient descent based on a variational calculation	21	Xeon, 3.06 GHz, 1 GB RAM	9, 27, 28
5	UCL	Hawkes, Crum	CC	Multiscale anisotropic fluid flow	Multiresolution using full multi-grid (FMG) with semicoarsening and implicit smoothing	300–480	Sun v20z Opteron 250, 2.4 GHz, 4 GB RAM	29
6	Lyon	Sarrut, Boldea		Demons with Gaussian regularization	Approximation of a second-order gradient descent	10	P4, 2.1 GHz 512 MB RAM	30, 31
7	McGill	Heath	CC	Free-form constrained by linear-elastic model	three-dimensional simplex	180–240	Suse Linux, 2.2 GHz Athlon, 1 GB RAM	32, 33
8	MD Anderson Cancer Center	Dong, Zhang		Demons with active force and multiresolution		0.75–2.3	Xeon, 2.8 GHz, 2 GB RAM	18, 34
9	Memorial Sloan Kettering Cancer Center	Mageras, Hu	SSD	Fast free form with energy minimization with vector field smoothness	Calculus of variations and Newton method	4.4–5.75	Xeon, 3.06 GHz, 2 GB RAM	13
10	Philips Medical Systems	Kaus, Vik	Surface matching	Thin plate spline		0.12–5*	Opteron 2.8 GHz, 8 GB RAM	35
11	Princess Margaret Hospital	Brock, Nguyen	Contour matching	Linear elastic finite element analysis		1.2–22*	Xeon, 3.73 GHz, 16 GB RAM	36-38

(*Continued*)

Table 3. List of participants: study number, institution, investigator, similarity metric used, interpolation method, optimization, and references (*Continued*)

Study no.	Institution	Investigator	Similarity metric	Regularization method	Optimization	Time (m)	Computer	Reference
12	Massachusetts General Hospital	Sharp	MSE	Cubic B-spline	Gradient descent	12–13	P4, 3.04 GHz, 1.5 GB RAM	39
13	University Hospitals K. U. Leuven	Van den Heuvel, Slagmolen	MI	B-spline	Limited memory quasi-Newton	44–61	2x Xeon, 2.8 GHz, 6 GB RAM	40
14	Varian Medical Systems	Nord	SSD	Demons		1.33–1.62	3.06 GHz dual Xeon, 8 GB RAM	N/A
15	Université Catholique de Louvain	Lee, Parraga	MSE	Multiscale demons + level set B-spline		60	P4, Xeon, 3.06 GHz, 4 GB RAM	41
16	University of Maryland	Shekhar, Wu	MSD	B-spline	Downhill simplex	540–618	Xeon 3.6 GHz, 2 GB RAM	42
17	University College of London	Hawkes, McClelland	SSD	B-spline	Gradient descent using finite difference	300	Sun v20z Opteron 250, 2.4 GHz, 4 GB RAM	43, 44
18	Netherlands Cancer Institute	Sonke, Wolthaus		Optical flow using quadrature filters		11	P4, 3.0 GHz, 1 GB RAM	45, 46
19	William Beaumont Hospital	Zhang, Chi	CC	Free form	Modified gradient search	3.5	Xeon, 2.8 GHz, 3 GB RAM	47
20	Tomographix IP Ltd	Dufort, Stundzia	SSD	Thin plate spline	Backward Euler gradient descent	26–76	P4, 3.2 GHz, 2GB RAM	N/A
21	U of Florida	Xia, Samant	SSD	Juggler algorithm (2 diffusion-based models)	Gradient descent	12	Intel 2.4 GHz, 3 GB RAM	48

Abbreviations: SSD = sum of the squared differences; MSD = mean square difference; CC = cross correlation; MSE = mean square error; P4 = Pentium 4; PD = Pentium D; CMS = CMS Software.
* Excludes contouring time.

Table 4. Results for the four-dimensional computed tomography lung data (mm)

		Thorax				Lungs only			
Study no.	Investigator	ABS AVG LR AP SI	ABS SD LR AP SI	MAX LR AP SI	Vector mag	ABS AVG LR AP SI	ABS SD LR AP SI	MAX LR AP SI	Vector mag
1	Noe, Tanderup	0.7	0.7	3.3	1.6	0.7	0.5	1.9	1.5
		0.8	1.2	6.4		0.8	1.1	6.4	
		1.2	1.5	7.5		1.0	1.4	7.5	
2	Han	0.6	0.5	2.6	1.1	0.5	0.4	2.0	1.1
		0.5	0.5	2.4		0.5	0.5	2.4	
		0.8	0.7	3.7		0.8	0.7	3.7	
3	El Naqa, Yang	0.8	0.8	3.0	1.6	0.7	0.5	2.6	1.4
		0.8	1.1	4.5		0.6	0.8	4.5	
		1.2	1.3	5.9		1.1	1.1	5.9	
4	Foskey, Chaney	0.8	0.8	3.5	1.7	0.7	0.6	2.8	1.5
		0.8	1.3	5.8		0.8	1.2	5.8	
		1.2	1.6	6.4		1.1	1.6	6.4	
5	Hawkes, Crum	0.7	0.5	2.4	1.5	0.7	0.6	2.4	1.4
		0.9	1.2	4.8		0.8	1.0	4.8	
		1.0	1.4	5.4		0.9	1.3	5.4	
6	Sarrut, Boldea	1.0	0.9	4.1	2.0	0.9	0.7	3.4	2.0
		1.2	0.9	4.2		1.2	1.0	4.2	
		1.3	1.8	7.7		1.3	1.9	7.7	
7	Heath	0.9	0.7	3.1	1.5	0.9	0.7	3.1	1.4
		0.9	0.8	3.7		0.9	0.6	3.7	
		0.8	1.2	4.6		0.7	1.1	4.6	
8	Dong	0.6	0.5	2.8	1.0	0.5	0.4	1.7	1.0
		0.5	0.5	2.6		0.4	0.4	1.8	
		0.7	0.6	2.9		0.7	0.6	2.9	
9	Mageras, Hu	0.8	0.6	2.5	1.6	0.8	0.6	2.5	1.4
		1.1	1.3	5.2		1.0	1.1	5.2	
		0.8	1.0	5.9		0.7	0.5	2.3	
10	Kaus, Vik	0.8	0.7	2.8	2.1	0.8	0.6	2.8	2.0
		1.4	1.5	6.9		1.3	1.2	6.9	
		1.3	1.3	7.2		1.2	1.3	7.2	
11	Brock, Nguyen	1.2	1.0	3.9	2.2	1.2	1.0	3.9	2.2
		1.4	1.3	6.5		1.5	1.3	6.5	
		1.3	1.3	6.7		1.1	1.0	4.1	
12	Sharp	1.1	0.9	4.7	2.0	1.1	0.9	4.7	1.9
		1.3	1.5	5.7		1.1	1.3	5.7	
		1.1	1.2	4.6		1.0	1.1	4.6	
13	Van den Heuvel	0.7	0.6	2.5	1.6	0.7	0.5	2.5	1.5
		0.8	0.9	4.0		0.7	0.8	3.5	
		1.2	1.7	7.2		1.2	1.8	7.2	
14	Nord	0.6	0.5	2.1	1.5	0.6	0.5	2.1	1.4
		0.9	1.4	5.7		0.8	1.1	5.7	
		1.0	1.3	5.6		0.9	1.2	5.6	
15	Lee, Parraga	0.7	0.6	2.3	1.6	0.7	0.6	2.3	1.5
		0.9	1.4	6.5		0.9	1.1	6.5	
		1.0	1.4	5.6		1.0	1.4	5.6	
16	Shekhar, Wu	1.2	1.1	5.5	3.0	1.2	1.2	5.5	3.0
		1.8	2.7	12.4		1.9	2.7	12.4	
		2.0	1.7	6.2		1.9	1.7	6.2	
17	Hawkes, McClelland	1.2	1.1	4.6	2.5	1.1	0.8	3.7	2.4
		1.4	1.3	7.0		1.5	1.2	7.0	
		1.7	2.0	7.8		1.5	1.9	7.8	
18	Sonke, Wolthaus	0.8	1.0	5.1	1.6	0.8	0.9	5.1	1.5
		0.9	1.6	7.8		0.9	1.3	7.8	
		0.9	1.1	4.2		0.8	1.0	4.0	
19	Zhang, Chi	0.8	0.7	3.0	1.8	0.8	0.7	3.0	1.6
		1.2	1.2	5.2		1.1	1.0	5.2	
		1.0	1.0	5.6		0.8	0.7	2.8	
20	Dufort, Stundzia	0.6	0.5	2.0	1.1	0.5	0.4	2.0	1.1
		0.6	1.1	5.1		0.6	0.9	5.1	

(*Continued*)

Table 4. Results for the four-dimensional computed tomography lung data (mm) (*Continued*)

		Thorax				Lungs only			
Study no.	Investigator	ABS AVG LR AP SI	ABS SD LR AP SI	MAX LR AP SI	Vector mag	ABS AVG LR AP SI	ABS SD LR AP SI	MAX LR AP SI	Vector mag
		0.8	0.8	4.0		0.8	0.7	4.0	
21	Xia, Samant	0.7	0.6	2.7	1.2	0.6	0.4	1.9	1.1
		0.7	0.8	3.2		0.6	0.7	3.2	
		0.7	0.5	2.0		0.7	0.5	2.0	

Abbreviations: ABS AVG = absolute average; ABS SD = absolute standard deviation, MAX = maximum; Vector mag = vector magnitude; AVG mag = average magnitude. LR = left–right; AP = anterior–posterior; SI = superior–inferior.

perform on multimodality images. The algorithms that submitted results had variable accuracy.

The prostate data were arguably the most challenging dataset because gas in the rectum caused artifacts and also substantial deformation of the prostate. Several participants declined to submit the results of their algorithms because of obvious erroneous results. Although the deformation exhibited in this patient is not typical, it is consistent with the deformation seen with the insertion of an endorectal coil. As MRI with endorectal coil becomes more common the

Table 5. Results for the four-dimensional computed tomography liver data (mm)

		Abdomen				Liver only			
Study no.	Investigator	ABS AVG LR AP SI	ABS SD LR AP SI	MAX LR AP SI	Vector mag	ABS AVG LR AP SI	ABS SD LR AP SI	MAX LR AP SI	Vector mag
1	Noe, Tanderup	1.5	1.2	5.0	6.7	1.4	1.0	3.6	8.2
		2.8	1.9	6.9		3.2	2.0	6.9	
		5.9	3.5	11.2		7.4	3.0	11.2	
2	Han	1.0	0.9	4.0	2.6	1.2	1.0	4.0	3.2
		1.2	1.3	5.9		1.5	1.5	5.9	
		2.0	2.5	10.1		2.6	2.8	10.1	
3	El Naqa, Yang	1.3	1.2	4.4	4.6	1.4	1.1	4.4	5.3
		2.4	1.7	5.8		2.8	1.8	5.8	
		3.7	2.2	7.8		4.3	2.0	7.8	
5	Hawkes, Crum	1.1	0.9	3.7	3.6	1.1	1.0	3.7	4.1
		1.7	1.5	5.9		1.8	1.7	5.9	
		3.0	2.0	6.6		3.5	2.1	6.6	
6	Sarrut, Boldea	1.1	0.9	3.3	4.8	1.2	0.9	3.3	6.0
		3.0	1.6	7.5		3.3	1.6	7.5	
		3.6	3.8	13.0		4.8	3.9	13.0	
7	Heath	0.8	1.0	5.9	1.7	0.9	1.2	5.9	1.8
		1.0	1.2	5.9		1.2	1.4	5.9	
		1.0	0.8	3.8		1.0	0.9	3.8	
8	Dong	1.1	0.9	4.4	2.3	1.2	1.0	4.4	2.6
		1.2	1.3	6.0		1.3	1.5	6.0	
		1.7	2.0	8.5		1.8	2.3	8.5	
9	Mageras, Hu	1.0	0.9	3.4	2.6	1.1	1.0	3.4	2.9
		1.4	1.4	6.4		1.5	1.6	6.4	
		1.9	1.1	4.0		2.2	1.2	4.0	
10	Kaus, Vik	1.1	1.0	3.4	2.1	1.2	1.1	3.4	2.3
		1.3	1.4	6.7		1.5	1.5	6.7	
		1.3	1.0	3.5		1.2	1.2	3.5	
11	Brock, Nguyen	1.2	1.1	4.0	2.4	1.2	1.0	4.0	2.3
		1.6	1.5	6.6		1.5	1.6	6.6	
		1.2	0.8	3.1		1.2	0.9	3.1	
12	Sharp	1.5	1.4	7.4	3.8	1.9	1.6	7.4	4.2
		2.6	1.9	7.4		2.6	2.2	7.4	
		2.4	1.5	5.2		2.7	1.6	5.2	
13	Van den Heuvel	1.2	1.1	4.8	3.1	1.5	1.2	4.8	3.8

(*Continued*)

Table 5. Results for the four-dimensional computed tomography liver data (mm) (*Continued*)

		Abdomen				Liver only			
Study no.	Investigator	ABS AVG LR AP SI	ABS SD LR AP SI	MAX LR AP SI	Vector mag	ABS AVG LR AP SI	ABS SD LR AP SI	MAX LR AP SI	Vector mag
		1.8	1.7	5.8		2.3	1.8	5.8	
		2.2	2.0	8.6		2.6	2.3	8.6	
14	Nord	1.1	0.9	3.3	3.3	1.1	0.9	3.3	4.0
		1.3	1.4	5.8		1.5	1.6	5.8	
		2.9	2.1	7.2		3.6	2.2	7.2	
16	Shekhar, Wu	1.1	0.9	3.8	3.4	1.3	1.0	3.8	4.1
		1.7	1.5	5.1		2.0	1.7	5.1	
		2.7	2.5	8.7		3.3	2.7	8.7	
18	Sonke, Wolthaus	1.3	1.3	6.2	2.3	1.5	1.4	6.2	2.6
		1.3	1.4	6.7		1.5	1.6	6.7	
		1.4	1.1	4.6		1.4	1.2	4.6	
20	Dufort, Stundzia	1.2	0.9	3.4	2.9	1.4	0.9	3.4	3.5
		1.8	1.5	5.7		2.2	1.6	5.7	
		1.9	1.5	6.2		2.4	1.7	6.2	

Abbreviations: ABS AVG = absolute average; ABS SD = absolute standard deviation, MAX = maximum; Vector mag = vector magnitude; AVG mag = average magnitude. LR = left–right; AP = anterior–posterior; SI = superior–inferior.

need to resolve these large deformations will become increasingly important. Additionally, the MR images were acquired at two separate times, unlike the 4D-CT datasets; therefore, they required a global image registration before the study of deformation. It was difficult for some investigators to return the total displacement vector, combining both the global shift and the deformation vector, and to validate whether the correct geometric transformation was combined properly. In future multicenter tests, a dry run with known shifts in the test dataset is highly recommended.

Algorithm implementation was shown to have an effect on the registration results. Three algorithms reported using Demons algorithm on the liver 4D-CT data, and the accuracy was 2.3, 3.3, and 4.8 mm. Three algorithms reported using thin-plate spline for the liver 4D-CT data, and the accuracy was 2.1, 2.9, and 7.8 mm; however, the similarity metric varied from contour matching (2.1 mm), sum of the squared difference (m = 2.9 mm), and feature of control points (m = 7.8 mm). Four algorithms reported using B-spline for the lung 4D-CT. Two algorithms used mean square error and had an error of 2.0 (optimized with gradient descent) and 3.0 mm (optimized with downhill simplex). One algorithm used SSD, error of 2.5 mm. The B-spline implementation, which used MI, had the smallest error (among the B-spline implementations) with an error of 1.6 mm. The clinical significance of these variations, and also the consistency of this accuracy across a larger number of patients, require further investigation.

In summary, this study highlights the success achieved in deformable registration for anatomic sites imaged with consistent contrast (*i.e.,* 4D-CT of the lung) and the work that must be done to ensure that these accuracies are also obtained for multimodality images and anatomy that has less contrast variation (*i.e.,* prostate). Maximum errors, which were large for some algorithms, should be investigated, and their effect on applications (*e.g.,* dose accumulation) should be studied.

Table 6. Results for the magnetic resonance imaging/computed tomography liver data (mm)

Study no.	Institution	Investigator	ABS AVG LR AP SI	ABS SD LR AP SI	MAX LR AP SI	AVG mag
2	CMS	Han	2.6	2.3	6.8	6.5
			5.0	1.4	6.6	
			2.2	1.6	5.4	
10	Philips Medical Systems	Kaus, Vik	1.1	0.9	2.5	4.5
			3.2	1.8	5.9	
			2.5	0.6	3.3	
11	Princess Margaret Hospital	Brock, Nguyen	1.5	1.3	3.5	3.9
			2.0	1.2	3.3	
			2.6	1.6	5.6	

Abbreviations: ABS AVG = absolute average; ABS SD = absolute standard deviation, MAX = maximum; Vector mag = vector magnitude; AVG mag = average magnitude. LR = left–right; AP = anterior–posterior; SI = superior–inferior; CMS = CMS Software.

Table 7. Results for the repeat magnetic resonance imaging prostate data (mm)

Study no.	Institution	Investigator	ABS AVG LR AP SI	ABS SD LR AP SI	MAX LR AP SI	AVG mag
8	MD Anderson Cancer Center	Dong	6.2	2.4	8.7	7.4
			3.1	2.0	5.4	
			2.0	1.5	3.6	
10	Philips Medical Systems	Kaus, Vik	0.5	0.4	0.9	4.3
			3.7	1.5	5.0	
			2.0	0.5	2.5	
11	Princess Margaret Hospital	Brock, Nguyen	1.0	0.3	1.2	2.3
			3.2	3.4	7.0	
			0.4	0.6	1.1	

Abbreviations: ABS AVG = absolute average; ABS SD = absolute standard deviation, MAX = maximum; Vector mag = vector magnitude; AVG mag = average magnitude. LR = left–right; AP = anterior–posterior; SI = superior–inferior.

REFERENCES

1. Brock KK, McShan DL, Ten Haken RK, *et al*. Inclusion of organ deformation in dose calculations. *Med Phys* 2003;30: 290–295.
2. Happersett L, Mageras GS, Zelefsky MJ, *et al*. A study of the effects of internal organ motion on dose escalation in conformal prostate treatments. *Radiother Oncol* 2003;66:263–270.
3. Koch N, Liu HH, Olsson LE, *et al*. Assessment of geometrical accuracy of magnetic resonance images for radiation therapy of lung cancers. *J Appl Clin Med Phys* 2003;4:352–364.
4. Mageras GS, Pevsner A, Yorke ED, *et al*. Measurement of lung tumor motion using respiration-correlated CT. *Int J Radiat Oncol Biol Phys* 2004;60:933–941.
5. Mattes D, Haynor DR, Vesselle H, *et al*. PET-CT image registration in the chest using free-form deformations. *IEEE Trans Med Imaging* 2003;22:120–128.
6. Rohlfing R, Maurer CR Jr, O'Dell WG, *et al*. Modeling liver motion and deformation during the respiratory cycle using intensity-based nonrigid registration of gated MR images. *Med Phys* 2004;31:427–432.
7. Schnabel JA, Tanner C, Castellano-Smith AD, *et al*. Validation of nonrigid image registration using finite-element methods: application to breast MR images. *IEEE Trans Med Imaging* 2003; 22:238–247.
8. Yan D, Jaffray DA, Wong JW. A model to accumulate fractionated dose in a deforming organ. *Int J Radiat Oncol Biol Phys* 1999;44:665–675.
9. Joshi SC, Miller MI. Landmark Matching via Large Deformation Diffeomorphisms, IEEE Transactions on Image Processing 2000;9.
10. Bharatha A, Hirose M, Hata N, *et al*. Tempany. Evaluation of three-dimensional finite element-based deformable registration of pre- and intraoperative prostate imaging. *Med Phys* 2001; 28:2551–2560.
11. Liang J, Yana D. Reducing uncertainties in volumetric image based deformable organ registration. *Med Phys* 2003;30: 2116–2122.
12. Wu X, Dibiase SJ, Gullapalli R, *et al*. Deformable image registration for the use of magnetic resonance spectroscopy in prostate treatment planning. *Int J Radiat Oncol Biol Phys* 2004;58: 1577–1583.
13. Lu W, Chen ML, Olivera GH, *et al*. Fast free-form deformable registration via calculus of variations. *Phys Med Biol* 2004;49: 3067–3087.
14. Brock KK, Sharpe MB, Dawson LA, *et al*. Accuracy of Finite Element Model (FEM)-Based Multi-Organ Deformable Image Registration. *Med Phys* 2005. In Press.
15. Rosu M, Chetty IJ, Balter JM, *et al*. Dose reconstruction in deforming lung anatomy: dose grid size effects and clinical implications. *Med Phys* 2005;32:2487–2495.
16. Venugopal N, McCurdy B, Hnatov A, *et al*. A feasibility study to investigate the use of thin-plate splines to account for prostate deformation. *Phys Med Biol* 2005;50:2871–2885.
17. Mohan R, Zhang X, Wang H, *et al*. Use of deformed intensity distributions for on-line modification of image-guided IMRT to account for interfractional anatomic changes. *Int J Radiat Oncol Biol Phys* 2005;61:1258–1266.
18. Wang H, Dong L, Lii MF, *et al*. Implementation and validation of a three-dimensional deformable registration algorithm for targeted prostate cancer radiotherapy. *Int J Radiat Oncol Biol Phys* 2005;61:725–735.
19. Keall PJ, Joshi S, Vedam SS, *et al*. Four-dimensional radiotherapy planning for DMLC-based respiratory motion tracking. *Med Phys* 2005;32:942–951.
20. Coselmon MM, Balter JM, McShan DL, *et al*. Mutual information based CT registration of the lung at exhale and inhale breathing states using thin-plate splines. *Med Phys* 2004;31: 2942–2948.
21. Kashani Rojano, Hub M, Balter JM, *et al*. Objective Assessment of Deformable Image Registration in Radiotherapy - a Multi-Institution Study. *Med Phys* 2009. In press.
22. Vandemeulebroucke J, Sarrut D, Clarysse P. The POPI-Model, a Point-Validated Pixel-Based Breathing Thorax Model. Toronto, Canada: International Conference on the Use of Computers in Radiation Therapy (ICCR); 2007.
23. Noe KO, Tanderup K, Lindegaard JC. GPU accelerated viscous-fluid deformable registration for radiotherapy. *Stud Health Technol Inform* 2008;132:327–332.
24. Thirion JP. Image matching as a diffusion process: an analog with Maxwell's demons. *Med Image Anal* 1998;2:243–260.
25. Pennec X, Cachier P, Ayache N. Understanding the Demon's Algorithm: 3D Non-Rigid Registration by Gradient Descent, 1999:597–506. LNCS 1679. Proc. of Medical Image Computing and Computer-Assisted Intervention (MICCAI'99).
26. Yang D, Lu W, Low DA, *et al*. 4D-CT motion estimation using deformable image registration and 5D respiratory motion modeling. *Med Phys* 2008;35:4577–4590.

27. Foskey M, Davis B, Goyal L, *et al*. Large deformation three-dimensional image registration in image-guided radiation therapy. *Phys Med Biol* 2005;50:5869–5892.
28. Christensen GE, Rabbitt RD, Miller MI. Deformable templates using large deformation kinematics. *IEEE Trans Image Process* 1996;5:1435–1447.
29. Crum WR, Tanner C, Hawkes DJ. Anisotropic multi-scale fluid registration: evaluation in magnetic resonance breast imaging. *Phys Med Biol* 2005;50:5153–5174.
30. Sarrut D, Boldea V, Miguet S, *et al*. Simulation of four-dimentional CT images from deformable registration between inhale and exhale breath-hold CT scans. *Med Phys* 2006;33:605–617.
31. Boldea V, Sarrut D, Carrie C. Comparison of 3D Dense Deformable Registration Methods for Breath-Hold Reproducibility Study in Radiotherapy. *In Proc SPIE Med Imaging* 2005; 5747:222–230.
32. Heath E, Collins DL, Keall PJ, *et al*. Quantification of a accuracy of the automated nonlinear image matching and anatomical labeling (ANIMAL) nonlinear registration algorithm for 4D CT images of lung. *Med Phys* 2007;34:4409–4421.
33. Collins DL, Holmes CJ, Peters TM, *et al*. Automatic 3-D model-based neuroanatomical segmentation. *Hum Brain Mapp* 1995;3:190–208.
34. Wang H, Dong L, O'Daniel J, *et al*. Validation of an accelerated 'demons' algorithm for deformable image registration in radiation therapy. *Phys Med Biol* 2005;50:2887–2905.
35. Kaus MR, Brock KK, Pekar V, *et al*. Assessment of a model-based deformable image registration approach for radiation therapy planning. *Int J Radiat Oncol Biol Phys* 2007;68: 572–580.
36. Brock KK, Dawson LA, Sharpe MB, *et al*. Feasibility of a novel deformable image registration technique to facilitate classification, targeting, and monitoring of tumor and normal tissue. *Int J Radiat Oncol Biol Phys*; 64:1245–1254.
37. Brock KK, Sharpe MB, Dawson LA, *et al*. Accuracy of finite element model-based multi-organ deformable image registration. *Med Phys* 2005;32:1647–1659.
38. Brock KK, Nichol AM, Menard C, *et al*. Accuracy and sensitivity of finite element model-based deformable registration of the prostate. *Med Phys* 2008;35:4019–4025.
39. Wu Z, Rietzel E, Boldea V, *et al*. Evaluation of deformable registration of patient lung 4DCT with subanatomical region segmentations. *Med Phys* 2008;35:775–781.
40. Byrd R, Lu P, Nocedal J, et al. A limited memory algorithm for bound constrained optimization. 1995;16:1190–1208.
41. Castadot P, Lee JA, Oarraga AX, *et al*. Comparison of 12 deformable registration strategies in adaptive radiation therapy for the treatment of head and neck tumors. *Radiother Oncol* 2008;89:1–12.
42. Shekhar R, Lei P, Castro-Pareja CR, *et al*. Automatic segmentation of phase correlated CT scans through nonrigid image registration using geometrically regularized free-form deformation. *Med Phys* 2007;34:3054–3066.
43. McClelland JR, Blackall JM, Tarte S, *et al*. A continuous 4D motion model from multiple respiratory cycles for use in lung radiatherapy. *Med Phys* 2006;33:3348–3358.
44. Rueckert D, Sonoda LI, Hayes C, *et al*. Nonrigid registration using free-form deformations: application to breast MR images. *IEEE Trans Med Imaging* 1999;18:712–721.
45. Wolthaus JW, Sonke JJ, van Herk M, *et al*. Reconstruction of a time-averaged midposition CT scan for radiotherapy planning of lung cancer patients using deformable registration. *Med Phys* 2008;35:3998–4011.
46. Hemmendorff M, Anderson MT, Kronander T, *et al*. Phase-based multidimensional volume registration. *IEEE Trans Med Imaging* 2002;21:1536–1543.
47. Zhang T, Chi Y, Meldolesi E, *et al*. Automatic delineation of on-line head-and-neck computed tomography images: toward on-line adaptive radiotherapy. *Int J Radiat Oncol Biol Phys* 2007;68:522–530.
48. Samant SS, Xia J, Muyan-Ozcelik P, *et al*. High performance computing for deformable image registration: towards a new paradigm in adaptive radiotherapy. *Med Phys* 2008;35: 3546–3553.